Sub-wavelength Imaging with Composite Metamaterials

Zsolt Szabó,[1, *]   Yasaman Kiasat,[2] and   Er Ping Li[2, †]

[1]*Department of Broadband Infocommunications and Electromagnetic Theory,*

Budapest University of Technology and Economics, Egry J. u. 18, 1111 Budapest, Hungary

[2]*Department of Electronics and Photonics, Institute of High Performance Computing,*

1 Fusionopolis Way, 16-16 Connexis, 138632, Singapore

compiled: February 5, 2014

After reviewing the requirements, which has to be satisfied by a metamaterial based sub-wavelength imaging systems a thin films lens is reported herein. The material of the lens is a composite of spherical Ag nanoparticles embedded in SiO_2 host material. The image of the lens is calculated, by solving the Maxwell equations, with the Transfer Matrix method. The procedure applies Maxwell-Garnet mixing rule and high frequency effective medium theory to calculate the electromagnetic parameters of the composite material. The formula of the composite material, the optimum working frequency and the thicknesses of the layers are determined by minimizing the absolute difference of the field distribution in the source and image planes. The details of the design procedure are presented and optimized configurations obtained under different constrains are discussed. The main advantage of the composite lens is that it can eliminate the hotspots present in the images of metallic superlens.

OCIS codes: (160.3918) Metamaterials; (310.6628) Subwavelength structures, nanostructures; (310.6805) Theory and design; (110.2990) Image formation theory.

1. Introduction

With the formulation of the optical diffraction criterion by Abbe at the end of the 19th century many researchers believed that the wavelength of light combined with the aperture size gives a final resolution of around 200 nm for optical microscopy [1]. In various fields of science, technology and medicine there is continuous need to obtain higher and higher resolution images. To date a broad range of microscopes based on very different principles and phenomena were developed and are researched for nanometer size resolution [2–4]. Sometimes the use of optical micro/nanoscopy presents exclusive way for imaging. For example living cells cannot be observed under electron microscopes and with X-rays, only when a low dose is sufficient.

Recently several research groups presents techniques to overcome the diffraction limit, to achieve superior resolution [5, 6]. Depending on the operating distance the sub-diffraction imaging techniques can be classified in far field or near field imaging methods. The far field methods as the stimulated emission depletion microscopy collects the optical signal far from the sample. The near field techniques collect the signal close to the sample including the evanescent components which decays at a very short distance from sample, but contains information which are needed for a complete reconstruction of

the image. For example in a near field scanning microscope (NSOM) a nano antenna is used to produce highly localized electric field intensity. When the probe is close to the sample the localized electromagnetic field can probe the sample producing optical response [7].

According to our observations magnetism vanishes at higher frequencies than the microwave regime for all natural materials, and the refractive index is always positive at optical frequencies [8]. The research of metamaterials has started with the goal of producing materials with negative refractive index i.e. simultaneous negative electric permittivity and magnetic permeability for imaging applications below the diffraction limit [9–11]. However the design of metamaterial lenses with negative refractive index is not an easy task. Despite of the extensive research efforts the existing optical metamaterial based imaging systems work only for narrow frequency range of plane waves incident with specific angle and polarization.

Metals has negative electric permittivity, therefore the main challenge of the metamaterial research is to produce the required negative magnetic properties. The metamaterial structures proposed in literature achieve the high frequency magnetism with sub-wavelength current loops or metallic structures, which can support anti-symmetric modes. The associated current flow produces a magnetic moment. A metamaterial with a customized optical response can be built as a superposition of resonant nano elements. With an advance in nano-fabrication there are possibilities to produce such

---

* Corresponding author: szabo@evt.bme.hu
† Corresponding author: eplee@ihpc.a-star.edu.sg

sub-wavelength structures. A very common design of an artificial material with tailored negative permittivity is the wire medium. The most common designs to produce artificial magnetism are the variations of the split ring resonators [12] and pairs of nano-rods [13]. The single wires and cut-wire pairs can be arranged in the so called fishnet geometries leading to structures with consecutive negative electric permittivity and magnetic permeability at optical frequencies [14]. However the metamaterial based imaging system will have a cutoff frequency due to unavoidable losses, and the finite size of the unit cell. As it is discussed in the next section, the required unit cell size can be estimated based on the frequency domain analysis of the image formation and the Nyquist-Shannon sampling criteria. The calculations indicate that 100 nm resolution requires unit cell sizes smaller than 20 nm. At this unit cell size, it remains a challenge to fabricate the required negative magnetic response.

In case of metamaterials constructed from small resonators the strength of the resonance decreases with the decrease of the unit cell size therefore for deep sub-wavelength resonators, the strength of the resonance is not strong enough to produce negative magnetic permeability. It seems that nano-structuring of metals cannot substitute magnetic charges; nevertheless resonator based double negative materials may find their applications as electromagnetic materials at higher wavelengths than the visible range. Consequently multilayer metal dielectric metal waveguide systems acting as double negative metamaterials working even in the ultraviolet range has been demonstrated [15, 16].

For imaging applications, to overcome the difficulties of producing double negative metamaterial, it was shown that a metamaterial with negative permittivity only is suitable for imaging transverse magnetic (TM) sources in the near field region [9, 17]. In the literature this type of material is referred as single negative metamaterial. In the experimental demonstration a 35 nm thick silver layer was used and leading to a resolution of about 65 nm [18]. Multilayer metal-dielectric systems were developed to increase the separation between the object and image plane. Far field imaging can be achieved with metal-dielectric multilayer arranged in cylindrical or hemispherical geometries [19, 20]. The double negative multilayer metal-dielectric-metal waveguide metamaterial provides full control over the electromagnetic components of light and it has been successfully applied for imaging two dimensional object in the ultraviolet [16].

The thin film metallic superlenses operate at the wavelength predefined by the metallic material of the lens, which corresponds to ϵ_r -1. The epsilon negative lenses are thin because the surface plasmon modes on the rear surface of the lens can only be excited by an input wave if the front and rear surfaces are strongly coupled [9]. However, it was found experimentally that for thin metallic films the surface roughness increases, which causes the

reduction of the image quality and may lead to hotspots in the image plane [21]. The hotspots are caused by the surface roughness of the outermost metallic layer, which builds the lens. Due to the few nanometer sized surface roughness, localized surface plasmons may be excited leading to extremely large electric field intensities, which can reach the image plane. Such hotspots are observable, see for example figure 4.b in [18], they can be reduced with advanced fabrication techniques [22], but not completely eliminated.

In this paper optimized lens designs are presented using single and multilayer thin film metal-dielectric composites. Colloidal chemistry can manufacture a large variety of nano-spheres with regular shapes at sizes of a few nanometers and there are well developed technologies to form thin layers of such inclusions. To design the composite lens, a transfer matrix based field solver, which is connected to a differential evolution optimization algorithm [23] is developed. The software package is freely available and the details of the design procedure are presented in this paper. Simplified expressions of the Maxwell-Garnett formula of layered spheres are derived to calculate the electric permittivity of composite materials. For spherical inclusions a high frequency extension of the Maxwell-Garnett mixing rule, which employs the dipole terms of Mie expansions is presented as well. The design formulas require the electric permittivity of metallic inclusions with averaged size of a few nanometers, therefore the change of the electric permittivity in function of size reduction is taken into account. The methodology is applied to design thin film lenses made of Ag spherical nanoparticles with average size of 5 nm dispersed in SiO_2 host. The working frequency, the filling fractions, the number and thickness of layers required to build an optimized composite lens for sub-wavelength imaging are provided.

2. Estimation of the unit cell size of metamaterials for sub-wavelength imaging

In order to investigate the requirements which has to be satisfied by metamaterial imaging systems the ideal arrangement composed of the metamaterial slab with refractive index $n = -1$ and thickness d, surrounded with air is considered. The source plane and the image plane is positioned at a distance $d/2$ in front and behind of the slab, as shown in Fig. 1(a). From system theory it is known that a system has ideal transmission if the transfer function has constant magnitude and linear phase. However metamaterials are sub-wavelength periodic structures, with finite sized unit cells and with unavoidable losses attributed to the building materials. Therefore the transfer function cannot be ideal and the imaging system will have a spatial cutoff frequency corresponding to the highest spatial harmonic, which can be passed. The bandwidth of the transfer function characterizes the quality of the metamaterial imaging system. In the following the transfer function of the ideal low pass filter is considered as the transfer function of the metamaterial imaging system as it can be seen in

Fig. 1(b). The intensity distribution in the image plane is calculated by convolving the Fourier transform of the source field with the transfer function and then performing inverse Fourier transform. The quality of the image, which is described by the absolute difference between the intensity distribution of the source and image, is investigated in function of the bandwidth of the transfer function.
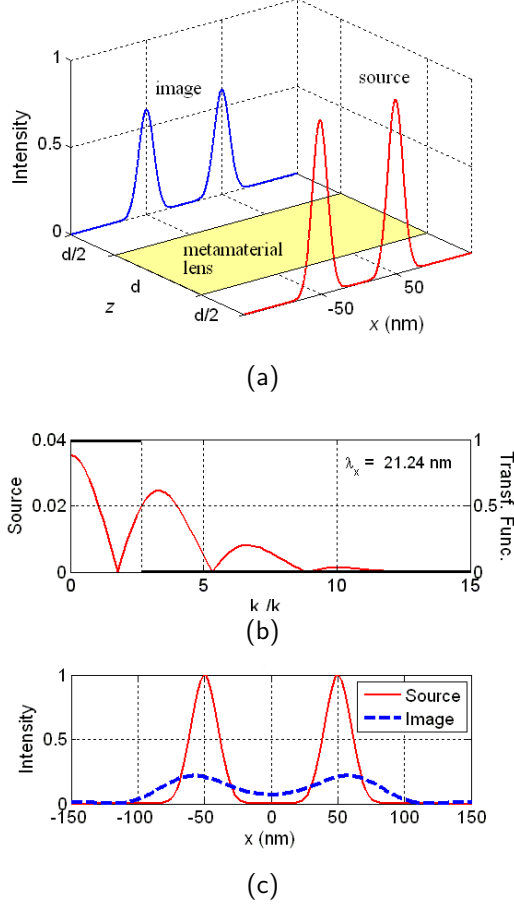

(a)

(b)

(c)

Fig. 1. (a) The metamaterial based imaging systems with the double Gaussian excitation, (b) the Fourier transform of the source and the Transfer Function, (c) the intensity distribution of the source and image; the highest spatial harmonic which is passed has a wavelength of 21.24 nm

The source to be imaged is the double slot illuminated with monochromatic light of 357 nm wavelength. The intensity distribution in the source plane can be approximated with a double Gaussian function. The half width of this source is 20 nm and the peeks are positioned 100 nm apart. The magnitude of the source Fourier transform is plotted in Fig. 1(b) with the read curve and the transfer function having cutoff at $k_x/k_0 = 2.674$ is plotted with the black line. The intensity distribution in the image plane is plotted in Fig. 1(c), and for reference the intensity distribution of the source plane is presented as well. Note that in the absence of the metamaterial the

two peeks are indistinguishable in the image plane and the parameters are configured in such a way that the two peeks can be distinguished only when evanescent components are transmitted. From the image the position of the two peeks can be distinguished with a proper threshold, however the magnitude and the half width of the source cannot be accurately obtained. The evolution of the absolute difference between intensity distribution of the source and image planes in function of the cutoff frequency of the transfer function is presented in Fig. 2.
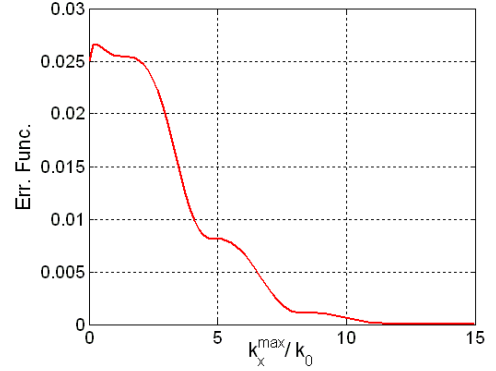

Fig. 2. The quality of the image in function of the bandwidth of the transfer function.

Passing more and more evanescent components, that is having larger and larger bandwidth of the transfer function improves the quality of the image. However,the Nyquist-Shannon sampling criteria indicates that the unit cell size of the metamaterial lens has to be smaller than half of the wavelength of the highest spatial harmonic transmitted by the system. In case of Fig. 1, the wavelength of the transmitted highest spatial harmonic is $\lambda_x = 21.24nm$. Therefore the required metamaterial unit cell sizes should be 10 nm or less in order to obtain the resolution of 100 nm with the source of 357 nm. The numerical methods to solve the Maxwell equations can also provide a guideline to estimate the required unit cell size. With the development of the Finite Difference Time Domain (FDTD) method extensive research has been performed to estimate the accuracy of the solution in function of the temporal and spatial discretization. The FDTD method requires four to ten times smaller unit cell sizes than the optical wavelength, to propagate plane waves in a homogeneous medium with acceptable accuracy over a distance of a few wavelengths. At this unit cell size, it remains a challenge to fabricate the required negative magnetic response from resonant elements.

3. Frequency domain analysis of metamaterial slab based imaging systems

With the advance of metamaterial research the theory of transmission and reflection of single and multilayer isotropic and anisotropic thin films [1] has been extended to materials with double negative metamaterials [9, 13].

In this section the main steps of the transfer matrix method for materials with positive and negative refractive will be reviewed with the purpose to present a reference for our freely available metamaterial lens designing software. The software can calculate the intensity distribution in the image plane (Fig. 1) for single and multilayer homogeneous composite lenses illuminated with arbitrary sources. The Fourier transform of the electromagnetic field distribution $g(x, y)$ of in the source plane is

$$G(f_x, f_y) = \int g(x, y) e^{-i2\pi(f_x x + f_y y)} dx dy \qquad (1)$$

where $k_x = 2\pi f_x$ and $k_y = 2\pi f_y$ are the components of the wave vector in the longitudinal direction, satisfying the relation $k_x^2 + k_y^2 + k_z^2 = \omega/c$, where k_z is the wavenumber in the transverse direction z, ω is the angular frequency and c is the speed of light in the medium which fills up the space in front of the lens. The algorithm in the present form is not taking any assumption how the source is generated, consequently there is no account for the interaction of the source and the metamaterial lens. The transfer function of the imaging system, in case of the double Gaussian source, which is independent of the spatial dimension y can be written as

$$T(k_x) = T_0(k_x) T_1(k_x) T_2(k_x) \qquad (2)$$

where $T_0(k_x) = e^{-ik_{z0}d_0}$ is the transfer function of the homogeneous medium with electric permittivity ϵ_{r0}, magnetic permeability μ_{r0} and thickness d_0, filling the space from the source plane to the lens; $T_2(k_x) = e^{-ik_{z2}d_2}$ is the transfer function of the homogeneous medium ϵ_{r2}, μ_{r2} and thickness d_2 filling the space from the lens to the image plane, and

$$T_1 = \frac{4\xi_1\xi_2}{(\xi_1+1)(\xi_2+1)e^{ik_{z1}d_1} + (\xi_1-1)(\xi_2-1)e^{-ik_{z1}d_1}} \qquad (3)$$

is the transfer function of the thin film lens with electromagnetic properties ϵ_{r1}, μ_{r1} and thickness d_1. The coefficients ξ_1 and ξ_2 depends on the polarization, in case of TM modes

$$\xi_1 = \frac{\epsilon_{r1}k_{z0}}{\epsilon_{r0}k_{z1}}, \quad \xi_2 = \frac{\epsilon_{r2}k_{z1}}{\epsilon_{r1}k_{z2}}, \qquad (4)$$

and in case of TE modes

$$\xi_1 = \frac{\mu_{r1}k_{z0}}{\mu_{r0}k_{z1}}, \quad \xi_2 = \frac{\mu_{r2}k_{z1}}{\mu_{r1}k_{z2}}. \qquad (5)$$

At this point it is worth to mention that the transfer function $T_1(k_x)$ depends on the material parameters not only through the coefficients ξ_1 and ξ_2, however implicitly through k_z as well. Fig. 3 summarizes the expressions of the transverse wavenumber k_z for different material parameters. As it can be observed from the table, when the lens is made of single or double negative metamaterial, the transverse component of the wave-vector k_z is imaginary and positive for evanescent waves, leading to amplification through the thickness of the lens. The dynamics of this process has been extensively discussed [24]. The field distribution in the image plane can be calculated by inverse Fourier transforming the convolution of the source Fourier transform multiplied by the transfer function as

$$g(x, y, z_2) = \int T(f_x, f_y) G(f_x, f_y) e^{i2\pi(f_x x + f_y y)} dx dy. \qquad (6)$$

The normalized absolute difference between the field distribution in the source and image planes measures the quality of the image

$$\Omega = \frac{1}{N_x} \sum_{j=1}^{N_x} |g(x_j, z_2) - g(x_j, 0)| \qquad (7)$$

where N_x is the number of points in the x direction. This expression serves as the objective function of the minimization procedure when the optimal lens parameters are determined.

	Propagating waves $k_x^2 \leq \frac{\omega^2}{c_0^2}\varepsilon_r\mu_r$	Evanescent waves $k_x^2 > \frac{\omega^2}{c_0^2}\varepsilon_r\mu_r$
$\varepsilon_r > 0$, $\mu_r > 0$	$k_z = \sqrt{\frac{\omega^2}{c_0^2}\varepsilon_r\mu_r - k_x^2}$	$k_z = -i\sqrt{k_x^2 - \frac{\omega^2}{c_0^2}\varepsilon_r\mu_r}$
$\varepsilon_r > 0$, $\mu_r < 0$		$k_z = i\sqrt{k_x^2 - \frac{\omega^2}{c_0^2}\varepsilon_r\mu_r}$
$\varepsilon_r < 0$, $\mu_r > 0$		
$\varepsilon_r < 0$, $\mu_r < 0$	$k_z = -\sqrt{\frac{\omega^2}{c_0^2}\varepsilon_r\mu_r - k_x^2}$	

Fig. 3. The transverse wavenumber k_z for different material parameters.

For multilayer metamaterial lenses the steps of the computational methodology are similar, except the calculation of the transfer function which is performed with the Transfer Matrix method. Applying the electromagnetic boundary conditions and taking into account the phase shift of the layers the following matrices can be assembled

$$M_m = \begin{bmatrix} \cos(k_z^m d_m) & i\frac{\omega\epsilon_r^m}{k_z^m}\sin(k_z^m d_m) \\ i\frac{k_z^m}{\omega\epsilon_r^m}\sin(k_z^m d_m) & \cos(k_z^m d_m) \end{bmatrix} \qquad (8)$$

where d_m is the thickness, ϵ_r^m is the electric permittivity and k_z^m is the wavenumber of the layer with index

m. Starting form the image plane the matrices M_m are multiplied together,

$$M = \prod_{m=n+1}^{0} M_m = \begin{bmatrix} M_{11} & M_{12} \\ M_{21} & M_{22} \end{bmatrix}. \quad (9)$$

The transfer function is given by the following expression

$$T(k_x) = \frac{2}{M_{11} + \frac{\omega \epsilon_r^0}{k_z^0} M_{21} + \frac{k_z^{n+1}}{\omega \epsilon_r^{n+1}} \left(M_{12} + \frac{\omega \epsilon_r^0}{k_z^0} M_{22} \right)}, \quad (10)$$

where k_z^0 is the wavenumber and ϵ_r^0 is the electric permittivity in front, while k_z^{n+1} is the wavenumber and ϵ_r^{n+1} is the electric permittivity behind the multilayer lens. The effective electric permittivity for the layers made of composite materials are approximated with mixing rules as it is presented in the next sections. In the presented methodology, the interactions between the inclusions of different layers are disregarded, and the electromagnetic material parameters of each layer is considered independent by the composition of any other layer.

4. Generalized Maxwell-Garnett formula for composites with layered spherical inclusions

The Maxwell-Garnett mixing formula [25] has been successfully applied to evaluate the electric permittivity of composite materials built of standalone spherical particles embedded in a homogeneous host materials. The Maxwell-Garnett formulas can be derived by replacing the spherical inclusions with static electric dipoles. The dipoles are excited by the external field and the dipole-dipole interaction is taken into account [26]. The theory has been extended to calculate the effective electric permittivity of composites formed by layered spheres in a homogeneous host medium [25]. The Maxwell-Garnett type mixing rules can be applied in case of individual spherical inclusions, which are much smaller than the guided wavelength for any statistical distribution of the particles as long as it is uniform and they do not agglomerate in clusters. The Maxwell Garnett mixing can be accurate at high density of inclusions [27, 28] and there is no requirement to arrange the inclusions in a regular lattice [26]. The typical composite, which can be characterized by the Maxwell-Garnett mixing rule, is shown in Fig. 4.
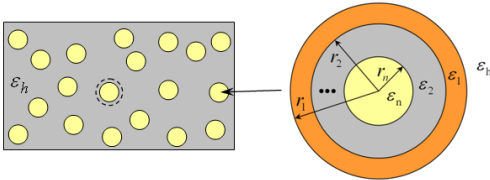

Fig. 4. Maxwell Garnett type composite with spherical multilayer inclusions.

Herein a recursive procedure is reported, which employs the Q_2 function

$$Q_2(x) = \frac{1-x}{1+2x}, \quad (11)$$

to substantially simplify the calculation of the effective electric permittivity of composites with arbitrary number of layers of the spherical inclusions. With the Q_2 function, the Maxwell Garnett formula of spherical inclusions takes the form

$$\epsilon_r^{eff} = \frac{\epsilon_r^h}{Q_2\left(\zeta Q_2\left(\frac{\epsilon_r^h}{\epsilon_r^i} \right) \right)} \quad (12)$$

where ϵ_r^h is the electric permittivity of the host material, ϵ_r^i is the electric permittivity of the spherical inclusion. Note that the size of the inclusions is not directly included in the Maxwell-Garnett formula and the filling factor ζ is the only geometry factor. In case of layered spherical inclusions, where the permittivity of the nth shells is ϵ_r^n (see Fig. 4), the effective electric permittivity of the composite is calculated with the iterative algorithm presented in Fig. 5. For layered spheres the mixing formulas depends on the ratio of the radius of neighboring shells. The iterative procedure reduces to the Maxwell-Garnett formula (12) in case of spherical inclusions.
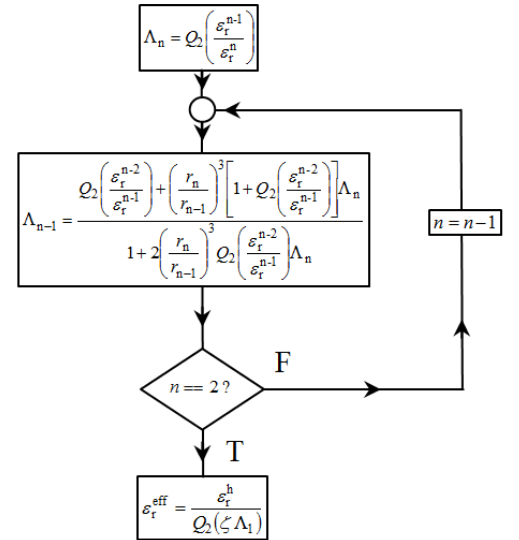

Fig. 5. Recursive algorithm to calculate the electric permittivity of Maxwell-Garnett type composites with multilayer spherical inclusions.

5. High frequency effective medium theory of spherical nanoparticles

The electrostatic approximation of the Maxwell Garnett formulas holds when the size of the inclusions is much

smaller than the guided wavelength. It is not straight-forward to decide when this condition is satisfied, because the quantity, which has to be compared with the particles size, is the guided wavelength in the composite, which depends on the effective refractive index. In this section a high frequency effective medium model of spherical inclusions is introduced [29, 30], which takes into account the scattering between the particles based on the theory of Mie scattering [31]. The scattering coefficients of the Mie expansion in case of standalone spherical particle, when the magnetic permeability of the particle and of the surrounding medium is the same can be expressed as

$$a_n = \frac{m\, \Psi_n\,(mx)\, \Psi_n'\,(x) - \Psi_n\,(x)\, \Psi_n'\,(mx)}{m\, \Psi_n\,(mx)\, \xi_n'\,(x) - \xi_n\,(x)\, \Psi_n'\,(mx)}, \quad (13)$$

$$b_n = \frac{\Psi_n\,(mx)\, \Psi_n'\,(x) - m\, \Psi_n\,(x)\, \Psi_n'\,(mx)}{\Psi_n\,(mx)\, \xi_n'\,(x) - m\, \xi_n\,(x)\, \Psi_n'\,(mx)}, \quad (14)$$

$$m = \frac{n_i}{n_h} = \frac{\sqrt{\epsilon_r^i \mu_r^i}}{\sqrt{\epsilon_r^h \mu_r^h}}, \quad x = \sqrt{\epsilon_r^h \mu_r^h}\, \omega\, r/c_0. \quad (15)$$

where Ψ and ξ are the Riccati-Bessel functions, the coefficient m is the ratio of the inclusion and host refractive index, ϵ_r^i and μ_r^i, ϵ_r^h and μ_r^h are the electric permittivity and magnetic permittivity of the inclusion and host, x is the size parameter, ω is the angular frequency of the incident light, r is the radius of the sphere and c_0 is the speed of light in vacuum. The electric and magnetic dipole polarizabilities can be expressed with the first terms of the scattering coefficients as [31]

$$\alpha_e = i\frac{3r^3}{2x^3}a_1, \ \alpha_m = i\frac{3r^3}{2x^3}b_1. \quad (16)$$

For standalone spheres these polarizabilities are exact for any size of the sphere and for any wavelength of the incident light. A high frequency extension of the Maxwell Garnett theory can be derived by introducing the polarizabilities (16) in the Clausius-Mossotti formula

$$\frac{\epsilon_r^{eff} - \epsilon_r^h}{\epsilon_r^{eff} + 2\epsilon_r^h} = \frac{\zeta}{r^3}\, \alpha_e, \quad (17)$$

leading to the following relations of the effective electric permittivity and magnetic permeability

$$\epsilon_r^{eff} = \frac{x^3 + 3\,i\,\zeta\,a_1}{x^3 - \frac{3}{2}i\,\zeta\,a_1}\, \epsilon_r^h, \ \mu_r^{eff} = \frac{x^3 + 3\,i\,\zeta\,b_1}{x^3 - \frac{3}{2}\,i\,\zeta\,b_1}\, \mu_r^h \quad (18)$$

The Riccati-Bessel functions and their derivatives for $n = 1$ can be easily expressed with elementary functions as follows

$$\Psi_1\,(\rho) = \frac{\sin\rho}{\rho} - \cos\rho,$$

$$\Psi_1'\,(\rho) = \sin\rho\left(1 - \frac{1}{\rho^2}\right) + \frac{\cos\rho}{\rho},$$

$$\xi_1\,(\rho) = \Psi_1\,(\rho) - i\left(\frac{\cos\rho}{\rho} + \sin\rho\right),$$

$$\xi_1'\,(\rho) = \Psi_1'\,(\rho) + i\left[\frac{\sin\rho}{\rho} - \left(1 - \frac{1}{\rho^2}\right)\cos\rho\right],$$

making the numerical evaluation of the effective electromagnetic parameters trivial.

6. Electromagnetic material parameters of the metamaterial lens

The proposed metamaterial lens is a composite material made of spherical metallic nanoparticles embedded in dielectric matrix. In this paper the spherical inclusions are silver (Ag) nanoparticles with averaged size of 5 nm and the dielectric host is glass (SiO_2). The size of the silver nanoparticles are larger that 2 nm, therefore quantum effects can be disregarded [32], however the electric permittivity of the nanoparticles must be modified due to size effects. In the following a classical model of the electric permittivity of silver is described as it is incorporated in the design procedure.

At optical frequencies, the electric permittivity of silver is determined not only by the motion of the free electrons in the lattice of metallic atoms, however the contribution of the bound electron vibration is also substantial. When the size of the metallic components is smaller than the mean free path of the conduction electrons (≈ 50 nm), the bulk electric permittivity of metals has to be modified to take into account the scattering of the conduction electrons form the particle boundary, which leads to an additional loss mechanism [31, 33]. The measured electric permittivity of the silver is obtained from the SOPRA database [34] as it is presented in Fig. 6.

The electric permittivity can be decomposed as

$$\epsilon_r = \epsilon_r^f + \epsilon_r^b, \quad (19)$$

where ϵ_r is the measured bulk electric permittivity, ϵ_r^f is the free electron and ϵ_r^b is the bounded electron contribution [33]. Note that the electric permittivity corresponding to bound electrons has been smoothed. The contribution of the free electrons to the electric permittivity is modeled with the Drude model

$$\epsilon_r^f = 1 - \frac{\omega_{pe}^2}{\omega^2 + i\gamma_e\omega}. \quad (20)$$

In this relation the plasma frequency ω_{pe} and the damping constant γ_e are determined form the measured bulk electric permittivity at a sufficiently low frequency,
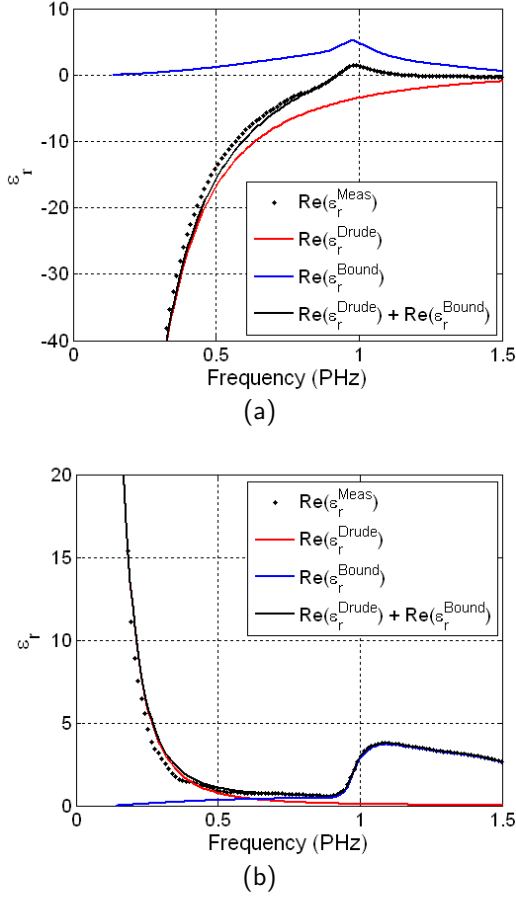
(a)

(b)

Fig. 6. Decomposition of the electric permittivity of Ag into free and bound electron contributions. In (a) the real part, while in (b) the the imaginary part of the electric permittivity is shown.

where the free electron motion is the major factor, which determines the electromagnetic properties

$$\omega_{pe} = \omega\sqrt{1 - \epsilon'_r + \frac{\epsilon''^2_r}{1 - \epsilon'_r}}, \tag{21}$$

$$\gamma_e = \omega\frac{|\epsilon''_r|}{1 - \epsilon'_r}, \tag{22}$$

where $\epsilon_r = \epsilon'_r + i\epsilon''_r$ is the electric permittivity at frequency $\omega << \omega_p$. For silver at frequency $f = 0.145$ PHz, the electric permittivity is $\epsilon_r = -206.23 + 30.64\,i$, which leads to the plasma frequency $\omega_{pe} = 13.2649$ rad/fs and damping constant $\gamma_e = 0.134793$ 1/fs. The bound charge contribution is calculated as

$$\epsilon^b_r = \epsilon_r - \epsilon^f_r, \tag{23}$$

and it is smoothed with spline interpolation to reduce the effect of the experimental errors. In Fig. 6 the real
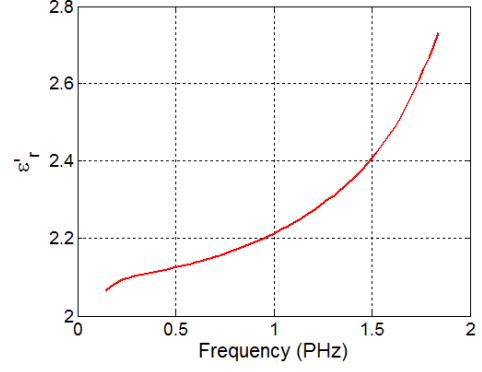

Fig. 7. The frequency dependent electric permittivity of the SiO$_2$ host material.

and imaginary part of the measured bulk electric permittivity and its decomposition into components, which depends on free and bounded electron contributions is shown. The size reduction effect on the electric permittivity is taken into account by modifying the damping constant in the Drude model [13]

$$\gamma_e = \gamma^{bulk}_e + \frac{v_F}{L_{eff}}, \tag{24}$$

where γ^{bulk}_e is the bulk value of the damping constant, $v_F = 1.4 \cdot 10^6$ m/s is the Fermi velocity of silver, and L is the effective mean free path to take into account the effect of collisions with the boundary of the nanoparticle. For particles with arbitrary shape the effective mean free path can be expressed with the billiard or Lambertian scattering model as $L_{eff} = 4V/S$, where V is the volume and S is the surface of the nanoparticle [35]. In particular, for spherical nanoparticles $L_{eff} = 4r/3$, where r is the radius of the nanoparticle, whereas for the spherical shell configuration the mean free path is $L_{eff} = 4\left(r^3_i - r^3_{i+1}\right)/3\left(r^2_i + r^2_{i+1}\right)$, where r_i and r_{i+1} are the radii of the outer and inner surfaces of the shell respectively [36].

The spherical nanoparticles are embedded in host dielectric material to form the composite. In this paper SiO$_2$ is considered as host material and the frequency dependent electric permittivity is obtained from the SOPRA database [34] and it is presented Fig. 7.

7. Composite lens made of silver nanoparticles embedded in SiO$_2$ host

The developed procedure is applied to design subwavelength imaging devices with composite materials. First single layer composite lenses with spherical inclusions are discussed. The primary parameters of the design procedure are the filling factor of the nanoparticles, the working frequency and the thickness of the lens, which are determine with optimization procedure. Constrains are enforced on the design parameters to obtain implementable composite parameters and to remain in the frame of the developed mixing rules.

In the following composite lens made of silver nanoparticles with a radius of 2 nm immersed in SiO_2 host is considered.Two composite material based imaging configurations are investigated. In the first configuration the thickness of the lens is 20 nm and it is surrounded with air. The source-lens and lens-image distances are 10 nm. In the second configuration the thickness of the lens is 30 nm and the surrounding material is SiO_2. The source-lens and lens-image distances are 15 nm. To understand the nature of the optimization problem in order to successfully design the metamaterial based imaging device the error surface of the objective function 7 is mapped. Fig. 8(a) and 8(b) presents the error function Ω, the absolute difference between the field distribution in the source and image planes, in function of the frequency and filling factor for the air-composite-air configuration and for the SiO_2-composite-SiO_2 case.

The maps of the objective function are extremely complex with several hills and walleyes and large flat regions, therefore gradient based optimizations fails to find useful parameters unless the optimization procedure is not started form the close proximity of the parameter regions where imaging is possible. Nevertheless the differential evolution based optimization [23] can be successfully applied for such objective functions. For the current problem a population size of 200-300 and maximum iterations of 100-200 are sufficient to converge to the proximity of the global minimum. The procedure requires to set searching interval for the variables of the optimization. The optimum frequency is searched in the interval $[0.4 \ldots 1]$ PHz. The lower limit of the filling factor is set to 0 but the upper limit is set successively to 0.2, 0.3, 0.4 and 0.5 for different instances of the optimization. The differential evolution algorithm converges to the upper limit of the filling factor. The marked points of Fig. 8(a) and 8(b) are the results of the optimization procedure obtained for the different constrains of the filling factor. The blue color indicates the regions where subwavelength imaging is possible, which is a thin curved valley in the space of the related frequencies and filling factors. The regions with high filling factors are outside of the range where the Maxwell-Garnett type mixing rules can produce accurate results and they are plotted only as reference, to join the case of the dense Ag thin film with filling factor $\zeta = 1$.

In Fig. 8(c) the transfer function of the 20nm thick composite lens (red) surrounded with air, filling factor $\zeta = 0.5$ and working frequency $f = 0.843$ PHz are presented, which corresponds to point 4 in Fig. 8(a). Fig. 8(e) presents the source, the image calculated with the Maxwell-Garnett and with the Mie scattering based effective medium theory. The size of the inclusions is deep sub-wavelength, therefore the high frequency mixing rule produces similar results as the Maxwell-Garnett theory, which approximates the metallic inclusions with static electric dipoles. For reference the transfer function and the image without the lens, which corresponds to a 40 nm thick air region is presented as well. The flat

portion of the transfer function of the air corresponds to the frequency region bellow cutoff where propagating waves are resent. In the absence of the lens the propagating waves can reach the imaging plane without any distortion, therefore for propagating components the magnitude of the transfer function equals one. The lens is not impedance matched consequently for the propagating components reflections occurs and the magnitude of the transfer function is less than one. In the absence of the lens the evanescent components are exponentially attenuated. The optimized lens can amplify several evanescent components and achieves higher resolution in the image plane. In Fig. 8(d) and 8(f) the transfer function and the image produced by the 30 nm thick composite lens surrounded with SiO_2, filling factor $\zeta = 0.5$ and working frequency $f = 0.79$ PHz are presented, which corresponds to point 4 in Fig. 8(b). The intensity distributions in the image plane in function of the filling factor are collected in Fig. 8(g) and 8(h). Increasing the upper limit of the filling factor in the optimization procedure the resolution of the image is improving and the optimum working frequency is shifting to higher values. The parameters of the lens corresponding to points 1-4 of Fig. 8(a) and 8(b) and the corresponding effective electric permittivity calculated by taking into account the size effect are summarized in Table 1. The simulations shows that with an increase in the filling factor the effective electric permittivity converges to values where the losses are minimum and the lens is impedance matched to the surrounding medium as much as it is possible.

Table 1. The filling factor, the frequency and the effective electric permittivity of the single layer composite lens

	Lens surrounded with air $d = 20$ nm			Lens surrounded with SiO_2 $d = 30$ nm		
	ζ	f (PHz)	ϵ_r^{eff}	ζ	f (PHz)	ϵ_r^{eff}
1	0.2	0.8036	$0.19 - 1.54i$	0.2	0.7744	$-0.28 - 2.42i$
2	0.3	0.8179	$-0.29 - 1.47i$	0.3	0.7791	$-1.18 - 2.35i$
3	0.4	0.8310	$-0.55 - 1.37i$	0.4	0.7842	$-1.72 - 2.14i$
4	0.5	0.8431	$-0.78 - 1.31i$	0.5	0.7906	$-2.01 - 1.91i$

The developed effective medium theory allows the calculation of the effective electric permittivity of spherical multilayer metal-dielectric inclusions. Three layered nano particles of Ag core, SiO_2 shell and Ag shell are considered as inclusions. The dimensions of the core and shells are set as optimization parameters along the filling factor and working frequency. The size effects are taken into account and the optimization converges to spherical Ag particles without any SiO_2 core. Note that turning off the size effects it is possible to obtain core shell configurations which perform better than the metallic nanoparticles, however for the considered dimensions in the range of ≈ 5 nm the additional losses due to the electron scattering on the core and shell boundaries cannot be disregarded.
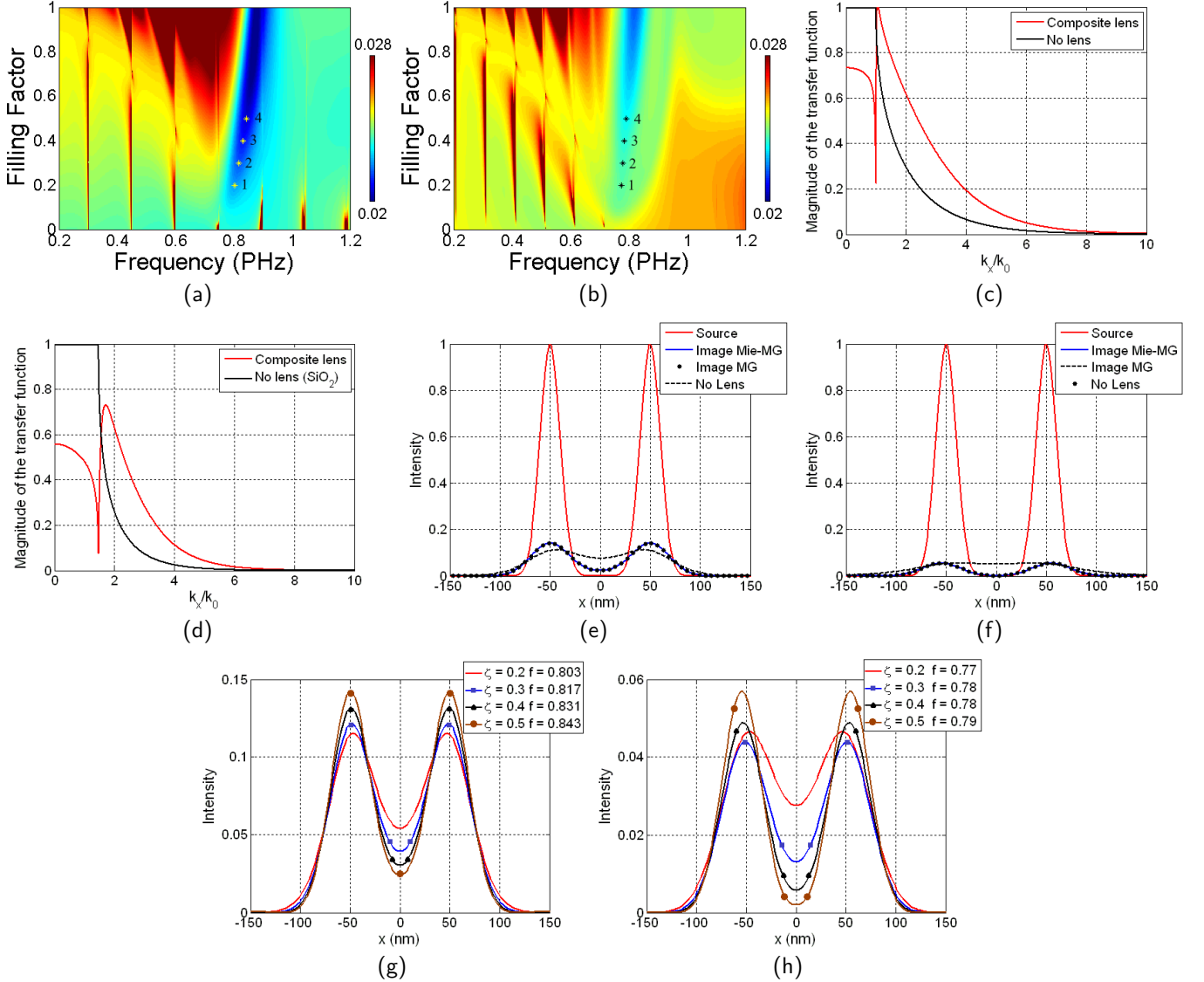
Fig. 8. Design of the imaging device with the single layer composite lens. The first column refers to the lens with thickness of 20 nm and and surrounded with air, while in the second column the the thickness of the lens is 30 nm and it is surrounded with SiO$_2$. The error function Ω, which is searched by the optimization procedure is presented in (a) and (b). The markers indicate optimized results obtained with constrains on the filling factor. The transfer function of the composite lenses are presented in (c) and (d). The intensity distribution in the source and image planes are plotted in (e) and (f). For reference the transfer function and the image without the lens are presented as well. The intensity distributions in the image plane corresponding to points $1-4$ of (a) and (b) are presented in (g) and (h).

The developed procedure is applied to design multi-layer lenses made of metallic composite and SiO$_2$ layers. The metallic composite is made of silver nanoparticles with a radius of 2 nm immersed in SiO$_2$ host. The medium in front and behind of the multilayer lens is air. The parameters of the optimization are the filling factor, the frequency and the thicknesses of individual layers. The searching intervals of the frequency and filling factor are set in a similar way as the bounds of the single layer lens. The number of composite layers is two or three and their thickness are optimized independently.

The first and the last layer of the lens is always made of composite material. In the optimization procedure the maximum value of the thickness of all individual layers, including the air regions in front and behind of the lens is set to 50 nm. The minimum thickness of the air regions is 5 nm, of the composite layers is 10 nm and of the SiO$_2$ separation layers is 5 nm or 10 nm respectively. The optimization returns the upper bound for the filling factor and the lower bound for the thicknesses. The design parameters of the multilayer lens are collected in Table 2. The third column presents the geometry pa-

rameters, where the thicknesses of the air regions are indicated with italic and the thickness of the composite layers with bold numbers. The absolute error between the intensity distribution in the source and image planes are presented in the forth column. For reference the effective electric permittivity of the designed composite material are included in the table.
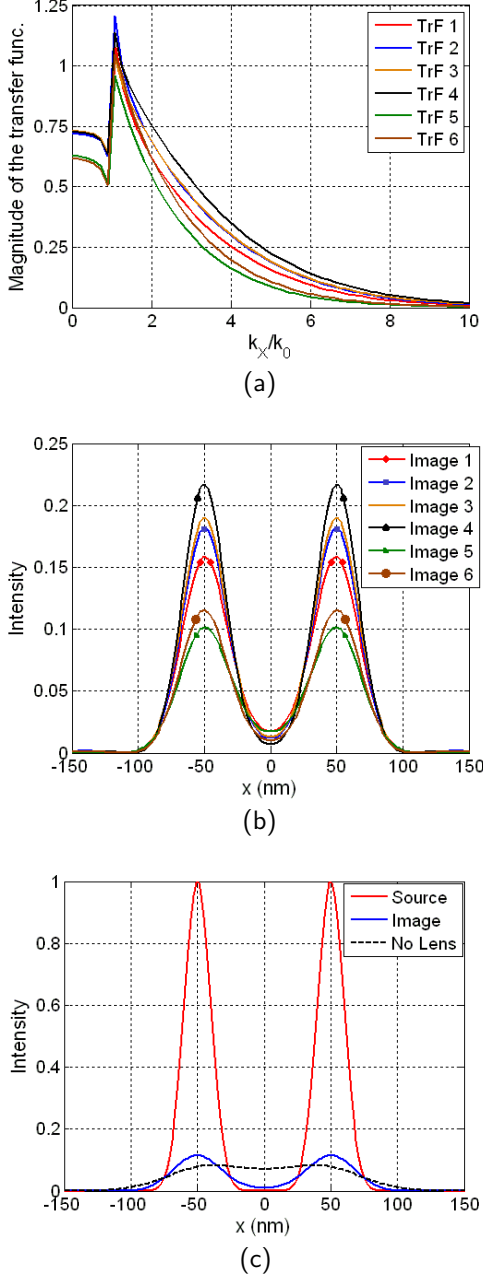

(a)

(b)

(c)

Fig. 9. Imaging with the multilayer lens. In (a) the transfer functions, and in (b) the images corresponding to the parameters presented in Table 2 are shown. The intensity distribution of the source and of the image for the lens, with parameters presented in the forth row of the table, along with the reference image without the lens are shown in (c).

Table 2. The design parameters of the multilayer lens

	ζ	f (PHz)	Thicknesses (nm)	Error $(\times 10^{-2})$	ϵ_r^{eff}
1	0.4	0.8171	*5* **10** 10 **10** *5*	1.98	$-0.85 - 1.54i$
2	0.5	0.8272		1.92	$-1.06 - 1.43i$
3	0.4	0.8235	*5* **10** 5 **10** *5*	1.89	$-0.72 - 1.46i$
4	0.5	0.8348		1.81	$-0.89 - 1.36i$
5	0.4	0.8227	*5* **10** 5 **10** 5 **10** *5*	2.16	$-0.73 - 1.47i$
5	0.5	0.8336		2.11	$-0.92 - 1.37i$

The imaging capabilities of the designed multilayer lenses with the parameters listed in Table 2 are presented in Fig. 7. The curves 1-4 refer to the composite-SiO$_2$-composite lens, while curves 5 and 6 to the composite-SiO$_2$-composite-SiO$_2$-composite lens. The transfer functions are presented in Fig. 9(a), and the intensity distributions of the image plane are plotted in 9(b). Similar to the single layer lens, the figures show increase of the resolution in function of the filling factor. The resolution is increased as well by decreasing the SiO$_2$ separation layer between the metallic composite films, therefore the highest resolution can be achieved with the layers 10 nm composite - 5 nm SiO$_2$ - 10 nm composite as it is plotted in Fig. 9(a). The separation between the source and image plane can be increased by adding more layers to the composite lens, which does not alters the shape of the transfer function considerably, only the magnitudes are reduced according to the additional losses.

8. Conclusions

Methodology to design single and multilayer flat metamaterial lenses has been presented. An estimate based on the frequency domain analysis of the image formation and the Nyquist-Shannon sampling criteria indicate that 100 nm resolution requires metamaterial unit cell sizes smaller than 20 nm. At this unit cell size, it is still a challenge to fabricate resonance based metamaterials. Therefore composite layers of Ag inclusions immersed in SiO$_2$ host are proposed as lens and implementable geometrical dimensions and composition has been determined with optimization.

These results support the use of *metallic composite-dielectric-metallic composite* waveguides for optical imaging application with high sub-wavelength spatial resolution. The composites can provide the tunability of the lens to the frequencies of commercially available laser sources. It may allow the acquisition of "colored" images that is changing the lens and imaging at different frequencies. When the radius of the inclusions is small compared to the wavelength the field enhancement between coupled metallic inclusions are not pronounced leading to uniform electromagnetic field distribution. Therefore metallic composites with deep sub-wavelength inclusions may eliminate the hotspots present in the images of metallic superlens. The multilayer composite superlens can offer a larger separation between the sources

and image, which can be critical for practical applications.

9. Acknowledgement

References

[1] M. Born and E. Wolf, *Principles of Optics: Electromagnetic Theory of Propagation, Interference and Diffraction of Light* (Cambridge University Press, 1999).

[2] W. E. Moerner, "Eyes on super-resolution," Nature Photonics **3**, 368 – 369 (2009).

[3] S. W. Hell, R. Schmidt, and A. Egner, "Diffraction-unlimited three-dimensional optical nanoscopy with opposing lenses," Nature Photonics **3**, 381 – 387 (2009).

[4] Y. Cotte, F. Toy, P. Jourdain, N. Pavillon, D. Boss, P. Magistretti, P. Marquet, and C. Depeursinge, "Marker-free phase nanoscopy," Nature Photonics **7**, 113117 (2013).

[5] S. W. Hell, "Far-field optical nanoscopy," Science **316**, 11531158 (2007).

[6] Z. Wang, W. Guo, L. Li, B. Lukyanchuk, A. Khan, Z. Liu, Z. Chen, and M. Hong, "All-angle negative refraction and active flat lensing of ultraviolet light," Nature Communications **2**, 16 (2011).

[7] S. Kawata, Y. Inouye, and P. Verma, "Plasmonics for near-field nano-imaging and superlensing," Nature Photonics **3**, 388 – 394 (2009).

[8] E. Palik, ed., *Handbook of Optical Constants of Solids I-IV* (Academic Press, 1985-1998).

[9] L. Solymar and E. Shamonina, *Waves in Metamaterials* (Oxford University Press, 2009).

[10] R. Marques, F. Martin, and M. Sorolla, *Metamaterials with Negative Parameters* (John Willey and Sons, 2008).

[11] C. Krowne and Y. Zhang, eds., *Physics of Negative Refraction and Negative Index Materials* (Springer, 2007).

[12] D. R. Smith, W. Padilla, D. C. Vier, S. Nemat-Nasser, and S. Schultz, "Composite medium with simultaneously negative permeability and permittivity," Phys. Rev. Lett. **84**, 4184 (2000).

[13] V. M. Shalaev, "Optical negative-index metamaterials," Nature Photonics **1**, 41–48 (2006).

[14] G. Dolling, M. Wegener, C. M. Soukoulis, and S. Linden, "Negative-index metamaterial at 780 nm wavelength," Optics Lett. **32**, 53–55 (2007).

[15] H. J. Lezec, J. A. Dionne, and H. A. Atwater, "Negative refraction at visible frequencies," Science **316**, 430–432 (2007).

[16] T. Xu, A. Agrawal, M. Abashin, K. J. Chau, and H. J. Lezec, "All-angle negative refraction and active flat lensing of ultraviolet light," Nature **497**, 470474 (2013).

[17] J. B. Pendry, "Negative refraction makes a perfect lens," Phys. Rev. Lett. **85**, 39663969 (2001).

[18] N. Fang, H. Lee, C. Sun, and X. Zhang, "Subdiffraction-limited optical imaging with a silver superlens," Science **308**, 534–537 (2005).

[19] J. Rho, Z. Ye, Y. Xiong, X. Yin, Z. Liu, H. Choi, G. Bartal, and X. Zhang, "Spherical hyperlens for two-dimensional sub-diffractional imaging at visible frequencies," Nature Communications **1** (2010).

[20] D. Lu and Z. Liu, "Hyperlenses and metalenses for far-field super-resolution imaging," Nature Communications **2** (2012).

[21] D. O. S. Melville and R. J. Blaikie, "Experimental comparison of resolution and pattern fidelity in single- and double-layer planar lens lithography," JOSA B **23**, 461–467 (2006).

[22] H. Liu, B. Wang, E. S. Leong, P. Yang, Y. Zong, G. Si, J. Teng, and S. A. Maier, "Enhanced surface plasmon resonance on a smooth silver film with a seed growth layer," ACS Nano **4**, 3139–3146 (2012).

[23] K. V. Price, R. M. Storn, and J. A. Lampinen, *Differential Evolution, A Practical Approach to Global Optimization* (Springer, 2005).

[24] R. Hegde, Z. Szabó, H. Yew-Li, E. P. L. Y. Kiasat, and W. J. R. Hoefer, "The dynamics of nanoscale superresolution imaging with the superlens," IEEE Trans. Microwave Theory and Techniques **59**, 2612–2623 (2011).

[25] A. Shivola, *Electromagnetic Mixing Formulae and Applications* (The Institute of Electrical Engineers, London, United Kingdom, 1999).

[26] D. E. Aspnese, "Local-field effects and effective-medium theory: A microscopic perspective," Am. J. Phys. **50**, 704–709 (1982).

[27] P. Mallet, C. A. Guérin, and A. Sentenac, "Maxwell-garnett mixing rule in the presence of multiple scattering: Derivation and accuracy," Phys. Rev. B **72**, 014205 (2005).

[28] V. Ossenkopf, "Effective-medium theories for cosmic dust grains," Astron. Astrophys. **251**, 210219 (1991).

[29] L. Lewin, "The electrical constants of a material loaded with spherical particles," Proc. IEE **94**, 65–68 (1947).

[30] R. Ruppin, "Evaluation of extended maxwell-garnett theories," Optics Communications **182**, 273279 (2000).

[31] C. F. Bohren and D. R. Huffman, *Absorption and Scattering of Light by Small Particles* (Wiley-VCH Verlag GmbH & Co. KGaA, 2004).

[32] H. Ehrenreich and H. R. Philipp, "Optical properties of ag and cu," Phys. Rev. **128**, 1622–1628 (1962).

[33] U. Kreibig, "Electronic properties of small silver particles: the optical constant and their temperature dependence," J. Phys. F: Metal Phys. **4**, 999–1014 (1974).

[34] www.sspectra.com/sopra.html.

[35] K. L. Kelly, E. Coronado, L. L. Zhao, and G. C. Schatz, "The optical properties of metal nanoparticles: the influence of size, shape, and dielectric environment," J. Phys. Chem. B **107**, 668677 (2003).

[36] A. Moroz, "Electron mean free path in a spherical shell geometry," J. Phys. Chem. C **112**, 1064110652 (2008).